Article citation info:
Berkache A, Ahmed AM, Qader FF, Amroune S, Mohamad BA. A combined experimental and CFD analysis of jet-crossflow interaction in turbine cooling passages. Combustion Engines. 0000;XXX(X):xx-xx. https://doi.org/10.19206/CE-226066

Amar BERKACHE
Aram Mohammed AHMED
Firas Faisal QADER
Salah AMROUNE
Barhm Abdullah MOHAMAD

Combustion Engines
Polish Scientific Society of Combustion Engines

A combined experimental and CFD analysis of jet-crossflow interaction in turbine cooling passages

ARTICLE INFO

Received: 23 May 2026
Revised: 27 June 2026
Accepted: 17 July 2026
Available online: 9 August 2026

This study presents a combined experimental and numerical investigation of the jet–crossflow interaction relevant to gas turbine blade film cooling applications. Four staggered rows of cylindrical cooling jets inclined at 30° are examined on a flat plate subjected to an incompressible crossflow with a mainstream velocity of 2 m·s⁻¹. Experiments were conducted at a fixed blowing ratio of M = 2 using Particle Image Velocimetry (PIV) to obtain time-averaged velocity fields and turbulence quantities across six measurement planes. Corresponding Reynolds-Averaged Navier-Stokes (RANS) simulations were performed using the standard k–ε and Shear Stress Transport (SST) turbulence models under identical boundary conditions. Quantitative comparisons of normalized axial and vertical velocity profiles (U/Ue and V/Ue) reveal that both turbulence models overpredict near-wall axial velocities in the jet exit region; however, the SST model shows consistently closer agreement with PIV measurements across streamwise locations ranging from X/D = −2 to X/D = 30. In the near-field region, the SST model captures jet penetration and mixing trends more accurately, whereas the k–ε model underestimates downstream jet diffusion and lateral spreading. Turbulent kinetic energy distributions further demonstrate that the SST model provides improved prediction of shear-layer turbulence intensity, although both models underestimate the spatial extent of turbulence compared to experimental data. The results indicate that, under the investigated conditions (M = 2, α = 30°), the SST model offers superior predictive capability for jet–crossflow interaction compared to the standard k–ε model, particularly in regions dominated by strong shear and recirculation. These findings guide RANS turbulence model selection.

Key words: *gas turbine blade cooling, film cooling, incompressible flow, jet interaction, turbulence modeling*

1. Introduction

The study centers on the analysis of film cooling performed on a test bench designed to mimic gas turbine blade-cooling scenarios. In the setup, the cooling air and hot air streams are kept at around 22°C and 40°C, respectively. The main aim is to investigate the formation and behavior of the cooling film generated by cold-air injection, which is essential for protecting turbine blades from high-temperature gases. The study is split across two primary parts: a numerical calculation and an experimental investigation.

Extensive literature research shows that significant effort has been put into understanding how film cooling works and how it interacts with the main flow. Among the many characteristics found to be significant are wall curvature, the three-dimensional structure of the outside flow, free-stream turbulence, blowing ratio, compressibility, flow unsteadiness, hole shape and location, and injection angle. Both numerical and experimental investigations have been used to assess these outcomes.

Obtaining a thorough understanding of flow patterns and heat transfer properties within turbine cascades is enabled by Computational Fluid Dynamics (CFD), a powerful tool that provides critical information for the design and optimization of gas turbines. Still, CFD models need to be validated with great care. This covers the selection of suitable turbulence models, the specification of precise inlet conditions, and grid independence tests. Local heat transfer has been shown to be especially sensitive to several variables related to secondary flows and, therefore, to the precision of physical and numerical modeling.

Under controlled conditions, experimental measurements are published for flat-plate designs, including specific Mach and Reynolds numbers and specified turbulence levels at the leading edge. Two-equation eddy viscosity models, such as k–ε and k–ω, remain widely used from a simulation perspective because they strike a balance between computational efficiency and accuracy. Particularly good at grasping near-wall behavior and transition to turbulence, both of which are essential for gas turbine uses, these models. Most film-cooling simulations reported in the literature are based on Reynolds-averaged Navier-Stokes (RANS) equations, which are time-averaged.

Experimental investigations by Andreopoulos and Rodi [3], Johnston et al. [17], and Cao et al. [9] have highlighted the complexity of the jet's near field, marked by large-scale coherent structures. These include jet shear layer vortices dominating the initial part of the jet, horseshoe vortices wrapping around the jet base, and counter-rotating vortex pairs induced by the momentum impact of the crossflow. The turbulence properties of the jet are much affected by these structures, which cause great jet distortion and the creation of wake vortices. Figure 1 offers a summary of the intricate flow field produced by the interplay between the crossflow and the jet.

For a baseline film cooling configuration, the predictive power of different RANS models is assessed against pertinent experimental data. Although RANS methods are still commonly used, many recent investigations have employed Large Eddy Simulation (LES) to better understand the complex flow patterns associated with film cooling.

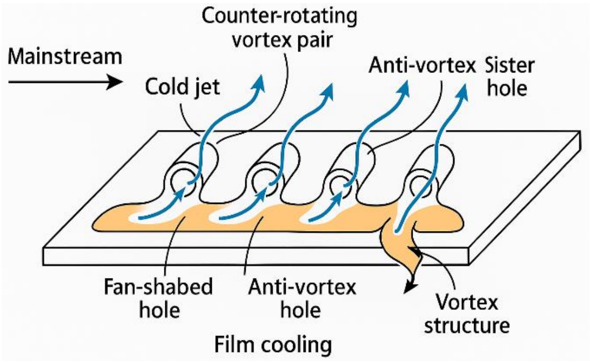

Fig. 1. Flow diagram of a row of jets based on experimental results

Yuan and Street's LES study [31] shows that a round jet discharge into a laminar crossflow is captured by large-eddy simulation. Their analysis effectively captures the coherent vortical structures observed in experimental studies, including the counter-rotating vortex pair (CVP), which emerges from the time-averaged action of sporadic vortical structures. Near the jet, wake vortices are also seen to form. The study also examines how commonly used simple boundary conditions affect simulation results and shows that the simulated mean flow fields match quite well with what is observed in real life. More recently, Leedom [20] examines how well film cooling performs using LES with different shapes for the coolant holes. The study examines discrete holes tilted at 35 degrees with a feeding plenum. The density ratio is 2, and the blowing ratios range from 0.5 to 2.0. Simulations are done for cylindrical holes with length-to-diameter ratios of 1.75 and 3.5, as well as for shaped holes (laterally diffused and console) with a ratio of 3.5, all of which come out into a laminar crossflow at a Reynolds number of about 16,000. Comparison with experimental data shows that the flow field and surface adiabatic effectiveness of the cylindrical holes are indeed correct. Important vortex structures, such as horseshoe, DSSN, and hairpin vortices, are resolved in the simulations. The findings show that jetting has a major impact on cooling performance; shaped holes, especially console holes, provide the best surface cooling. Still, in terms of aerodynamic loss, cylindrical and console holes beat out horizontally distributed ones.

In another study, Balaji et al. [5] examined how pin fins with different diameters and heights affect cooling efficiency at the corners of an aircraft turbine blade tip. Furthermore, Wang et al. [27] conducted a numerical investigation of the influence of four distinct hole layouts on film-cooling effectiveness and particle build-up on a curved surface. They investigated particle deposition using the RNG k–ε turbulence model, along with a discrete-phase model implemented using user-defined functions, to assess capture and impact efficiencies. The research showed that, at a blowing ratio of 1.2, combined fan-shaped and round-to-slot holes enhanced average film-cooling performance by 69.8% and 60.3%, respectively, compared with conventional cylindrical holes. Except for the round-to-slot hole, the inclination angle between 30° and 45° strongly affected cooling performance. Particle size also influenced capture and impact efficiencies, which at blowing ratios between 0.3 and 0.9 rose, then fell. The fan-shaped and round-to-slot holes had the lowest efficiencies at a 30° tilt angle, whereas for 1 μm particles, the round-to-slot hole had the best.

To assess film-cooling efficiency, Xiaojian He et al. [16] compared the pressure-sensitive paint (PSP) and thermochromic liquid crystal (TLC) approaches. The same wind tunnel was used to test both methods across sixteen scenarios with different mainstream Reynolds numbers (35,000, 45,000, and 57,000), blowing ratios (0.5, 1.0, 1.5, and 2.0), and density ratios (0.91 and 1.44). According to the research, their cooling efficiency measurements showed certain differences, even if both PSP and TLC found an ideal blowing ratio at low to medium Reynolds numbers. Heat transmission in the solid region was thought to be responsible for these differences. Increased heat transfer was observed at high mainstream Reynolds numbers and blowing ratios, but at high Reynolds numbers and low blowing ratios, the impact declined. PSP and TLC results virtually matched under low blowing ratio (0.5) and nitrogen-cooling conditions, suggesting that at low blowing and density ratios, heat conduction effects are small.

Targeting a concave surface resembling the leading edge of a gas turbine blade, Forster and Weigand [14] conducted an experimental and numerical investigation of jet-impingement cooling. The study included nine circular jets, each encircled by three film-cooling holes arranged in a staggered pattern. Experiments at a Reynolds number of 30,000 varied the jet-to-surface separation distance and considered the impacts of crossflow. The study assessed heat transfer distributions utilizing TLC methods, whereas OpenFOAM was used to conduct complementary RANS calculations with the k-ω SST turbulence model. Crossflow was shown to lower total heat transfer and stagnation point but to produce a more consistent distribution of heat. Shorter jet separation distances also magnified crossflow effects and raised general heat transfer rates. The numerical calculations successfully caught regional flow events and fit well with empirical data. Yao et al. [30], who examined the effects of hole form, also verified this tendency. Their research revealed that non-cylindrical hole shapes provide better cooling effectiveness, particularly at lower blowing ratios (M = 0.5).

Using LES, Yao et al. [30] examined whether large turbulent structures formed when the injection ratio, M, was 1.7. The coolant and mainstream flows had the same volume of fluid. Their simulation results showed strong agreement with experimental data, validating the model's reliability.

By using triangular thin plates and a flop arrangement to alter the orientation of cylindrical film-cooling holes, Choi et al. [11] conducted experimental studies to improve film-cooling efficiency. The study examined several rows of 35° angled cylindrical holes in a low-speed wind tunnel at a Reynolds number of 196,167 and blow ratios ranging from 0.3 to 2.0. The authors examined several arrangements using thermographic and flow visualization methods. At a blowing ratio of 1.0, the baseline cylindrical holes had a cooling effectiveness of about 0.1. However, even in the downstream area, the inclusion of the triangular-shaped thin plate-flop greatly increased film coverage and stopped flow separation. With only an 8% increase in discharge coefficient, this design showed up to a 242.7% improvement in cooling effectiveness over conventional cylindrical holes, making it the best option for gas turbine uses.

Toghraie et al. [25] looked at the dynamic viscosity of a magnetite-based nanofluid (Fe_3O_4/water) between 20 and 55°C in another study. The data revealed that while viscosity decreases with increasing temperature, it increases significantly with increasing nanoparticle volume fraction, reaching a maximum improvement of 129.7%. To accurately forecast the viscosity of this nanofluid, a new correlation was proposed.

Esfe and Toghraie [13] also investigated how thermoelectric cooling (TEC) affected the performance of solar stills. According to their research, freshwater output is directly related to the strength of solar radiation. Using TEC on the glass surface of the still boosted freshwater production by 15% to 62%, therefore showing the promise of this enhancement approach for solar desalination devices. The research by Pouya Barnoon et al. [6] examines how flow behavior and heat transfer in a porous chamber are affected by heating and cooling generators and cryogenic conductors. Using the Finite Volume Method (FVM), the simulations were run with single-phase and two-phase models to forecast heat transfer behavior. The Newtonian, incompressible, and constant working fluid – a water–copper oxide nanofluid is thought of. Several cases with the volume fraction kept constant were studied to evaluate the rate of heat transmission and simplify the distribution. To explain fluid flow and thermal behavior inside the porous medium, the Darcy-Forchheimer model was used. Data revealed that cryogenic conductors improve heat transfer, and heating and cooling generators improve thermal performance. But in particular circumstances, traditional porous containers performed more effectively. Using current thermal control methods, the study's main goal was to maximize heat transmission efficiency.

Table 1. Summary of key studies on flow, heat transfer, and cooling

Authors	Research focus	Methods and tools	Key contributions and findings
Guo et al. [15]	Heat-transfer enhancement in jet impingement with surface protrusions.	CFD-based solver and experimental measurements; comparison of smooth, spherical, ellipsoidal, and teardrop protrusions; parametric analysis of Reynolds number, protrusion height, and spacing.	Ellipsoidal protrusions offer the highest cooling performance; they raise the average Nusselt number by 15% compared to smooth surfaces. Increasing protrusion height by 22% further improved heat transfer without raising pressure losses; lowering protrusion spacing improved cooling with pressure-loss variations under 5%. Suggested a passive augmentation plan for turbine blade cooling with low penalties.
Wang et al. [28]	Effect of rectangular jet aspect ratio (AR) on the jet-in-crossflow (JICF) flow and energy transfer.	Wind tunnel experiments, LES and turbulence analysis, temperature-field analysis, coherent vortex identification.	By delaying the onset of the hanging vortex breakdown, it was shown that increasing AR greatly improves jet penetration (46.4% gain at X/d = 1). Recognized the counter-rotating vortex pair (CVP) as a pseudo-sequential vortex structure. Greater AR helps stabilize downstream vortices, reduce temperature swings, accelerate turbulent kinetic energy decay, and thereby boost energy dissipation by 28.8%. The study offers guidance on maximizing jet-orifice design to improve industrial cooling and mixing efficiency.
Chatzistefanou et al. [10]	Performance analysis of a precooled air-breathing propulsion system.	One-dimensional thermodynamic modeling.	Demonstrated the importance of bypass duct modeling for improving engine efficiency and fuel economy.
Jones and Wille [18]	Simulation of a plane jet in cross-flow using LES.	LES with artificial inflow and wall boundary conditions; Smagorinsky-Lilly, one-equation, and dynamic subgrid models.	Mesh adapted to the mean velocity field improves resolution; reasonable agreement with experimental results; minor differences observed between residual-scale models.
Berkache and Rabah [8]	Film cooling analysis in gas turbine blades.	3D simulations in Fluent applied k–ε, RSM, and Shear Stress Transport (SST) turbulence models; experimental validation with Particle Image Velocimetry (PIV).	RSM improves predictions over other RANS models; RANS limitations, due to isotropic eddy diffusivity, lead to overpredictions of the centerline cooling velocity.
Kong et al. [19]	Swirling jet flow and heat transfer in the turbine blade leading-edge chamber.	Numerical simulation with varying jet hole offsets (e/d), jet spacing (H/d), and different dimple geometries (SDs, OTDs) at Re = 30,000.	A jet hole offset enhances heat transfer by 15%; OTDs in a staggered arrangement yield a 24% improvement in thermal-hydraulic performance; dimples increase the area but reduce the average Nusselt number.
Vicano et al. [26]	Examined the flow characteristics of a jet in crossflow issuing from a 777-shaped cooling hole under different velocity ratios.	PIV, Refractive Index Matching (RIM), NaI-water working fluid, turbulence statistics, vorticity analysis.	Given a thorough experimental characterization of velocity fields, Reynolds stresses, turbulence intensity, and vortex development for velocity ratios ranging from 0.4 to 1.2. Determined the main vertical structures produced by the 777-shaped aperture and measured turbulence growth downstream from the hole exit. The findings provide better knowledge of complex cooling-hole designs for improved jet mixing.
Yang et al. [29]	Temperature uniformity in array jet impingement cooling.	Detailed flow and thermal field analysis under maximum cross-flow; vortex structure investigation.	Identified entrainment and counter-rotating vortex-induced nonuniformities; increasing Reynolds number or reducing spacing improves uniformity; implications for turbine cooling design.

In a linked study, Barnoon et al. [7] examined the cooling behavior, stress distribution, and displacement properties of proton exchange membrane fuel cells (PEMFCs) under natural and forced convection. The goal of the research was to lower operating temperature, thermal stress, and deformation by maximizing the quantity and thickness of bipolar plates. Results showed that forced convection decreased the working temperature by over 30 K, therefore considerably lowering the number and thickness of the plates. Natural cooling could pose thermal risks to the system while speeding up plate heating.

In another study, Baghoolizadeh et al. [4] examined how to best use energy in homes, particularly in air conditioning systems. Building models were simulated employing the EnergyPlus program under several climatic scenarios. Five main design factors were selected, and for each city, 300 Design of Experiments (DOE) points were evaluated. Constructing predictive models from the simulation data involved using Response Surface Methodology (RSM). The outcomes showed a 2% to 16% decrease in related expenses and total energy load. Significant gains were also noted in the Human Heating Comfort and Static Payback Period measures, therefore highlighting the efficiency of the optimization approach.

The objective of this research is to experimentally and numerically investigate the interaction between multiple staggered cooling jets and a turbulent crossflow representative of gas turbine blade film cooling conditions. PIV measurements are employed to quantify the mean velocity fields and turbulence characteristics of four rows of jets inclined at 30° and operating at a blowing ratio of M = 2. In parallel, RANS simulations using the standard k–ε and SST turbulence models are performed under identical operating conditions. The study aims to evaluate the ability of these turbulence models to accurately predict jet penetration, lateral spreading, near-wall flow behavior, and the distribution of turbulent kinetic energy by direct comparison with experimental data. Ultimately, the research seeks to identify the most suitable turbulence model for reliable CFD prediction of jet-crossflow interactions in turbine blade film cooling applications.

2. Problem statement

While experimental tests on the interaction between a main airflow and a secondary cooling flow over a flat wall with several holes have been conducted, the main goal of these geometric setups is to spread the cooling jet more uniformly across the surface, thereby improving overall cooling effectiveness and uniformity. The experimental tests took place in the ISAE-ENSMA wind tunnel facility, which is part of the P′ Institute in Poitiers, France. This was accomplished by fitting a flat plate with a number of offset rows of holes. The test plate in Figures 2 and 3 has 81 cylindrical cooling holes set in staggered rows. They show how the ISAE-ENSMA tunnel is configured and how the plate is set up. Every hole has a 6 mm diameter and is angled 30° from the wall surface. The holes also have elliptical edge exits that measure 12 mm across. This is supposed to help the jet attach better and make the film cooler.

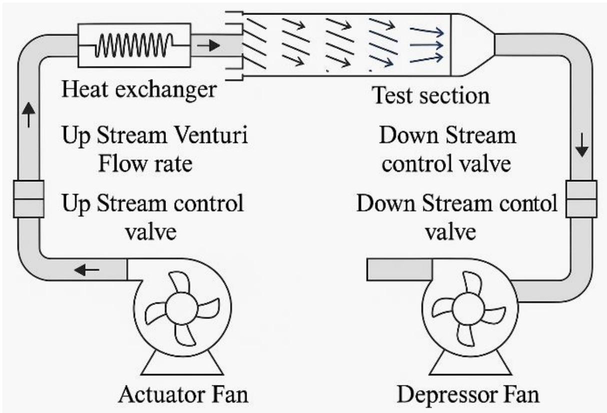

Fig. 2. General description of the tunnel facility

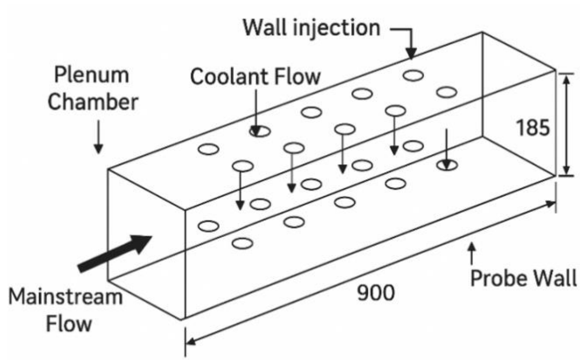

Fig. 3. General description of the test vein and the flat plate

PIV measurements were performed using a flat-plate configuration intersected by four rows of open coolant jets. As shown in Fig. 4, the jets were angled at 30° toward the axial direction and had a consistent blowing ratio of M = 2 during the experiments carried out at the ENSMA test facility. In the (x, y) plane, both the injection flow and the main flow are present. For data acquisition, the flat plate is split into six measurement planes. The camera system can move along the z-axis within the (x, z) plane. There is a 35 mm displacement between each measurement plane. This helps the camera capture the three-dimensional flow structure well.

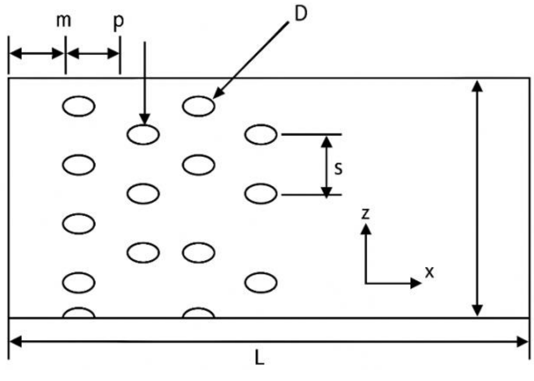

Fig. 4. Calculation domain and experimental setup

Figure 5 illustrates the six measurement planes delineated within the experimental test facility. Data acquired from these planes are used to assess the accuracy of numerical predictions from RANS simulations conducted under equivalent operating conditions. Two turbulence modeling approaches are investigated: the standard k–ε model and the SST model, aiming to identify the model that exhibits superior agreement with the experimental measurements. In this configuration, the primary flow propagates along the x-axis at a uniform velocity of 2 m/s, while the coolant jets are introduced at an inclination of 30° relative to the x-axis within the (x, z) plane.

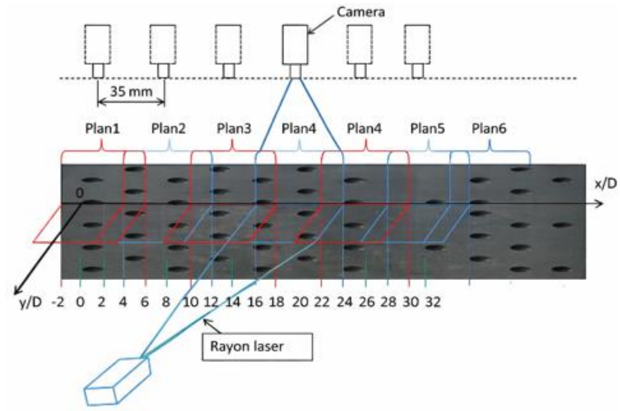

Fig. 5. Measurement plans available with PIV

3. Methodology

3.1. Experimental apparatus and protocol

To investigate the effect of secondary jet flows on the main airflow in gas turbine blade cooling, a sophisticated experimental setup was painstakingly built at the Laboratory for Thermal Studies (LET) of ENSMA in Poitiers. The experimental configuration mostly consists of a flat plate with a main airstream flowing across it. Secondary jets are pushed through several rows of staggered holes in the plate, and they interact with the main airstream. As seen in Fig. 6, the system has a PIV for high-resolution velocity field measurements. The device has these basic parts:

a) The main airflow is generated by a MEIDINGER high-performance fan, model HP 98 / 10–13, with a static pressure of 20,000 Pa
b) A test section with 81 cylindrical holes spaced 30° apart from the surface and measuring 6 mm in diameter houses a multi-perforated plate
c) A test section with 81 cylindrical holes spaced 30° apart from the surface and measuring 6 mm in diameter houses a multi-perforated plate
d) A test section with 81 cylindrical holes spaced 30° apart from the surface and measuring 6 mm in diameter houses a multi-perforated plate
e) A flow regulation valve for fine-tuning the injection parameters of the secondary air jets.

3.2. Integrated flow rate and velocity monitoring system

Located upstream of the test section, the main flow control system includes a regulatory valve (Fig. 7) that monitors the mass flow rate of the principal airflow, denoted Q_e. Located downstream of the test section, a secondary flow control system is used to measure the suction flow rate, Q_d, which matches the injection flow rate, Q_i, as shown in the diagram. Dedicated flow control systems help to control and track the mass flow rate of every stream. Each system has a control valve to regulate flow to the intended setpoint, as well as a Venturi meter for accurate flow rate measurement. To precisely measure airflow velocity, the Venturi devices are connected to both absolute and differential pressure sensors. While the injection flow rate varied, reaching a maximum of 25 g/s, the primary flow mass rate was kept steady at 45 g/s throughout all tests.

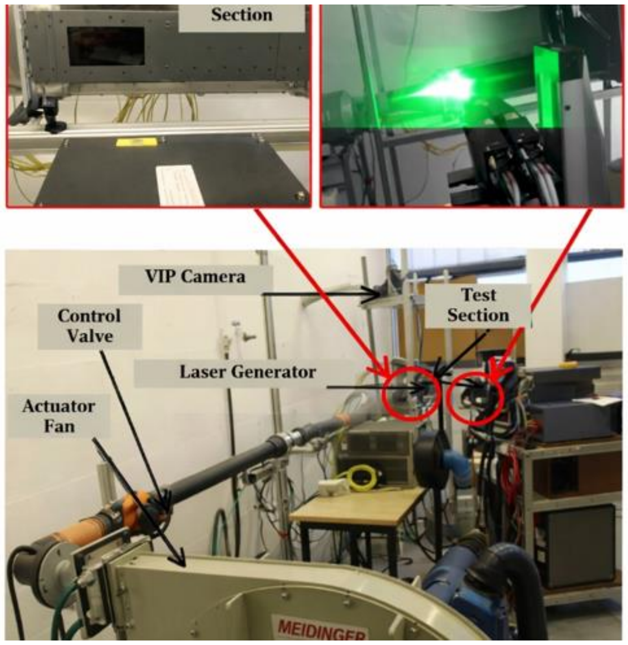

Fig. 6. Experimental apparatus

3.3. Aerodynamic conditions

Defined and determined using the following equation, the main aerodynamic parameter controlling this experimental study is the blowing ratio MM:

$$M = \frac{\rho_i U_i}{\rho_e U_e} \tag{1}$$

In this formulation, ρ_e, U_e, U_i, and ρ_i denote the density and velocity of the main flow, and the velocity and density of the injection flow, respectively. Accordingly, the blowing ratio MM can also be expressed in the following alternative form:

$$M = \frac{\rho_i U_i\,(nS_i)}{\rho_e U_e S_e} \times \frac{S_e}{nS_i} \tag{2}$$

where S_i is the injection area which is calculated by:

$$S_i = \frac{\pi D^2}{4} \tag{3}$$

Se: represents the tunnel test section (Se = 0.0185m^2), n: is the number of open injections.

The main mass flow rate and the injection flow rate are calculated by the relations below:

$$Q_e = \rho_e U_e S_e \tag{4}$$

$$Q_i = \rho_i U_i (nS_i) \tag{5}$$

These calculations reveal a link between the injection rate M and the primary flow rate Q_e as well as the injected air flow rate Q_i:

$$M = K\frac{Q_i}{Q_e} \text{ with } K = \frac{S_e}{nS_i} \tag{6}$$

where Q_i is the mass flow rate of the injection flow (kg·s^{-1}), Q_e is the mass flow rate of the main flow (kg·s^{-1}).

For all analyzed cases, the main mass flow rate is set to 45 g·s^{-1}, corresponding to an average mainstream velocity of 2 m·s^{-1}. Therefore, the mass flow rate of the coolant injection stream controls the blowing ratio (M).

3.4. Mathematical formulation

The numerical model was validated by a thorough CFD analysis. Among other important factors, this process involved selecting a suitable turbulence model, defining precise inlet boundary conditions, and evaluating grid independence. Among the several engineering-relevant outputs, the local heat transfer distribution is particularly sensitive to the complex dynamics of secondary flow structures. Therefore, its precise prediction relies much on the accuracy of the computational approach used and the underlying physical modeling, as well as its robustness. The Navier-Stokes equations, given here, are the governing equations for fluid flow [1, 2, 12, 22-24, 29]:

$$\frac{\partial \overline{\rho u_i}}{\partial x_j} = 0 \tag{7}$$

$$\bar{u}_j \frac{\partial \overline{\rho u_i}}{\partial x_j} = -\frac{\partial \bar{p}}{\partial x_i} + \frac{\partial}{\partial x_j}\left[\rho\nu\left(\frac{\partial \bar{u}_i}{\partial x_j} + \frac{\partial \bar{u}_j}{\partial x_i}\right) - \rho\overline{u_i{}'u_j{}'}\right]$$

where: $-\rho\,\overline{u_i'u_i'}$ are the Reynolds turbulent stresses.

3.5. Standard k–ε model

In the standard k–ε model, the Reynolds stresses are modelled as:

$$-\rho\overline{u_i{}'u_j{}'} = -\frac{2}{3}\rho k\delta_{ij} + 2\mu_t\overline{S_{ij}} \tag{8}$$

The eddy viscosity μ t is related to the turbulent kinetic energy k and to its dissipation rate ε as

$$\mu_t = \rho C_\mu \frac{k^2}{\varepsilon} \tag{9}$$

(9)

All standard linear two-equation turbulence models are based on Eq. (8), which shows a linear relationship between the Reynolds (turbulent) stress tensor and the mean strain rate tensor. Solving their respective modelled transport equations yields the spatial distributions of the turbulent kinetic energy (k) and its dissipation rate (ε) inside the flow field. These equations include the following source terms:

$$S_k = P - \varepsilon \quad ; \quad S_\varepsilon = C_{\varepsilon 1}\frac{\varepsilon}{k}P - C_{\varepsilon 2}\frac{\varepsilon^2}{k} \tag{10}$$

where P is the production of turbulence

$$P = -\rho\overline{u_i{}'u_j{}'}\frac{\partial \bar{u}_i}{\partial x_j} \tag{11}$$

Thus, the velocity field's near-wall boundary conditions are defined using the usual wall-function technique. A Dirichlet condition requiring a zero value at the wall is used for the (k). By contrast, a local equilibrium assumption underpins the (ε) at the neighboring near-wall node, hence guaranteeing coherence with the wall-function approach, as:

$$\varepsilon = C_\mu{}^{3/4}\frac{k^{3/2}}{0.4\delta y} \tag{12}$$

3.6. Shear Stress Transport (SST) model

Menter [21] created the SSTs turbulence model by carefully combining the best features of the k–ε and k–ω models to maximize their efficacy throughout various flow zones. To be more precise, the SST model uses the k–ω formulation in the near-wall region, where it is known to work well, and then switches to the transformed k–ε equations in the free-stream region, where the latter model usually provides better accuracy. A mixing function, F1, controls this change by gently interpolating between the two formulations. As Tulapurkara observes, the SST model improves its ability to capture the impacts of unfavorable pressure gradients and separation by combining Bradshaw's idea that the Reynolds shear stress is correlated with the turbulent kinetic energy [30, 31]. The resulting transport equations of the SST model are as follows:

$$\frac{\partial}{\partial t}(\rho k) + \bar{u}_j\frac{\partial}{\partial x_j}(\rho k) = \tau_{ij}\frac{\partial \bar{u}}{\partial x_j} - \beta^*\rho\omega k + \frac{\partial}{\partial x_j}\left[(\mu + \sigma_k\mu_t)\frac{\partial k}{\partial x_j}\right] \tag{13}$$

$$\frac{\partial}{\partial t}(\rho\omega) + \bar{u}_j\frac{\partial}{\partial x_j}(\rho\omega) = \frac{\mu}{\mu_t}\tau_{ij}\frac{\partial \bar{u}}{\partial x_j} - \beta\rho\omega^2 + \frac{\partial}{\partial x_j}\left[(\mu + \sigma_\omega\mu_t)\frac{\partial \omega}{\partial x_j}\right] + 2(1 - F_1)\rho\sigma_{\omega 2}\frac{1}{\omega}\frac{\partial k}{\partial x_i}\frac{\partial \omega}{\partial x_j} \tag{14}$$

The constants in the SSTs turbulence model are determined using a blending function. If φ represents a generic constant in the SST model, and φ_1 and φ_2 are the corresponding constants in the original k–ω model and the transformed k-ε model, respectively, then φ is computed as follows:

$$\varphi = F_1\varphi_1 + (1 - F_1)\varphi_2 \tag{15}$$

The constants in the k–ω are:

$\sigma_{k1} = 0.850$, $\sigma_{\omega 1} = 0.5$, $\beta_1 = 0.0750$, $a_1 = 0.311$, $\beta^* = 0.090$, $K = 0.410$

$$\gamma_1 = \frac{\beta_1}{\beta^*} - \frac{\sigma_{\omega 1}K^2}{\sqrt{\beta^*}} \tag{16}$$

The constants in the transformed k-ε model are:

$\sigma_{k2} = 1.0$, $\sigma_{\omega 2} = 0.856$, $\beta_2 = 0.0828$, $\beta^* = 0.09$, $K = 0.41$,

$$\gamma_1 = \frac{\beta_2}{\beta^*} - \frac{\sigma_{\omega 2}K^2}{\sqrt{\beta^*}} \tag{17}$$

τ_{ij} is given by Equation:

$$-\rho\overline{u_i{}'u_j{}'} = -\frac{2}{3}\rho k\delta_{ij} + \mu_t\left(\frac{\partial \bar{u}_i}{\partial x_j} + \frac{\partial \bar{u}_j}{\partial x_i}\right)$$

$$F_1 = \tanh(\arg_1{}^4): \tag{18}$$

$$\arg_1 = \min\left[\max\left(\frac{\sqrt{k}}{0.09\omega y}, \frac{500\nu}{y^2\omega}\right), \frac{4\rho\sigma_{\omega 2}k}{CD_{k\omega}y^2}\right] \tag{19}$$

$$CD_{k\omega} = \max\left(2\rho\sigma_{\omega 2}\frac{1}{\omega}\frac{\partial k}{\partial x_j}\frac{\partial \omega}{\partial x_i}\ ,\ 10^{-10}\right), \nu_t = \frac{a_1 k}{\max(a_1\omega, \Omega F_1)} \tag{20}$$

$$F_2 = \tanh\left(arg_2^{\,2}\right)$$

$$arg_2 = \mathrm{Max}\left(2\frac{\sqrt{k}}{0.09\omega y}, \frac{500\nu}{y^2\omega}\right) \tag{21}$$

3.7. Computational domain and boundary conditions

The three-dimensional numerical flow field is shown in Fig. 7 using a symmetry plane that mimics the arrangement of the ISAE-ENSMA test facility. The computational domain consists of a flat plate with four rows of spaced cylindrical cooling holes. Each hole has a diameter of 6 mm. In the transverse (s/D = 4) and axial (p/D = 4) directions, the hole spacing ratio is fixed at 4. Using a three-dimensional steady-state formulation, the commercial CFD program FLUENT solves the governing transport equations. Figure 7 illustrates the mesh, geometry, and boundary conditions (BC) applied for both the experimental and computational investigations.

To guarantee accuracy in resolving convective terms, a 2nd order upwind discretization diagram is used. Ambient air comprises both the injected coolant jet and the mainstream flow in the current film-cooling configuration. The working fluid is treated as a perfect gas inside a macroscopic continuum framework because the thermodynamic conditions are somewhat low, that is, the temperature and pressure are both moderate.

The elliptic nature of the governing partial differential equations makes it essential to define boundary conditions along the entire boundary of the computational domain. Three different forms of boundary conditions, velocity inlet, outflow, and symmetry constraints, are applied as seen in Fig. 7. The coolant jet is introduced at an inclination angle (α) of 30°, with an injection slot width (D) of 0.006 m. The accurate representation of turbulent flow within CFD models depends on the correct specification of inlet parameters for important variables: the axial (u) and transverse (v) velocity components, turbulent kinetic energy (k), and either the turbulence dissipation rate (ε) or specific dissipation rate (ω), which jointly define the inflow conditions. These criteria are derived from pertinent experimental data sets [3]. The axial and vertical components of velocity are exactly specified at the jet exit interface; the spanwise velocity is considered to be insignificant. The axial velocity distribution is defined alongside the turbulence intensity variables at the inlet region upstream of the flat plate. At the upstream and downstream borders of the domain, a zero-gradient (Neumann) condition is applied for all remaining flow quantities.

Three different mesh resolutions are contrasted in Fig. 8: coarse, intermediate, and fine. Derived from the k–ε turbulence model at the station X/D = 0, the findings center on the normalized axial mean velocity profiles U/U_e. Two particular mesh setups are emphasized: a coarse mesh with 557,381 cells and a fine mesh with 2,575,501 cells. The goal of this mesh sensitivity analysis was to find the best mesh that would yield accurate results while requiring the least computer time. It also aimed to see how mesh density affected simulation accuracy.

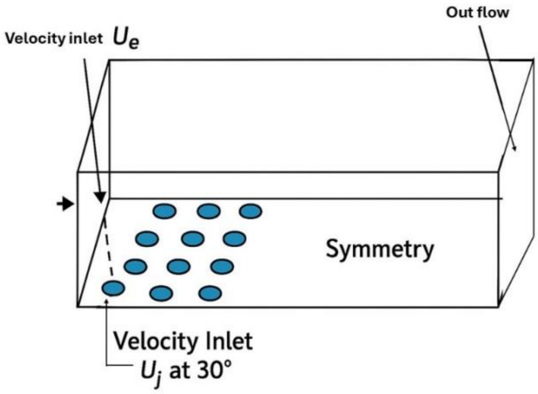

Fig. 7. Experimental and numerical studies: 3-D domain and boundary conditions

The comparison shows that the coarse and fine meshes have practically identical normalized velocity profiles, indicating mesh independence in the near-field. Therefore, the coarse mesh was chosen for the following simulations to cut computer time without compromising accuracy. Using the three-dimensional CFD commercial solver, ANSYS FLUENT and the SIMPLEC pressure-velocity coupling method, the governing transport equations were found and solved. To better control numerical stability and accuracy, the convective terms were discretized using a second-order upwind scheme.

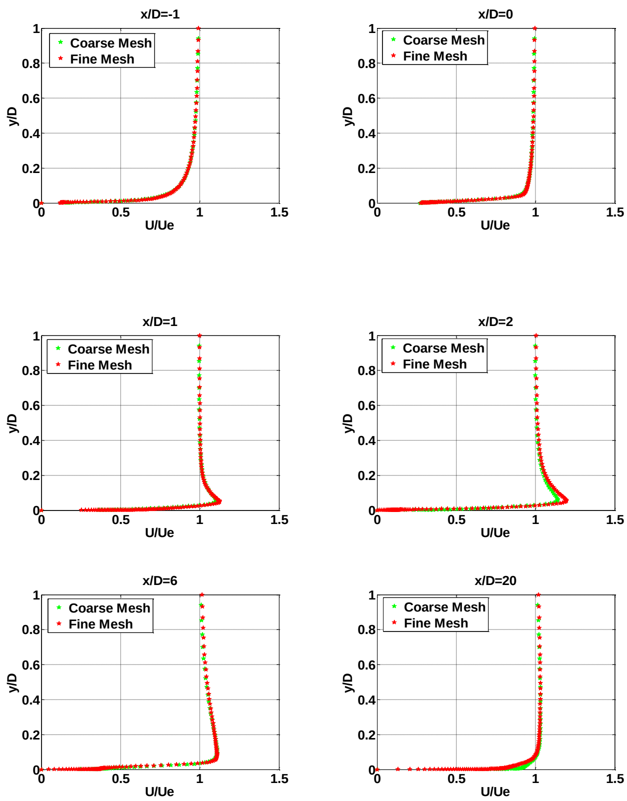

Fig. 8. Profiles of the average reduced axial speeds U/Ue obtained by the model turbulence k–ε for two coarse and fine meshes

Except at the downstream point (x/D = 20), where modest differences were observed, the profiles of the normalized axial velocity U/Ue remained constant across the assessed stations for the two mesh resolutions. These differences are due to numerical accuracy rather than mesh quality. Therefore, all the following computations were carried out using a coarse mesh with about 24,000 cells.

3.8. Mesh and computational domain

The two-dimensional (2D) variant of the CFD commercial solver, ANSYS FLUENT, was used to model and solve the transport equations. The flat plate domain had a structured, non-uniform mesh applied. Two different mesh arrangements were tested to determine a suitable mesh resolution. The first had roughly 24,000 cells; the second, around 38,000. Finer resolution near the wall showed grid spacing up to ten times smaller in that area.

The comparative study revealed few differences in the findings from the two mesh setups, suggesting that the smaller near-wall mesh had little effect on accuracy. As a result, the coarser mesh with less refinement near the wall was chosen for all subsequent simulations to reduce computational cost and time. Figure 9 shows the last mesh layout.

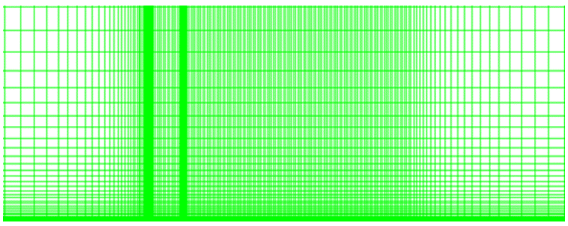

Fig. 9. Mesh of the plane plate

4. Results and discussion

4.1. Results analysis

To evaluate the predictive correctness of the numerical method, representative results of the time-averaged flow field derived from both PIV measurements and RANS simulations are compared in the present study. To determine the most appropriate turbulence model, FLUENT, a commercial CFD program, is used to simulate turbulent flow across a flat plate. Two often-used k–ε turbulence model equations are assessed. The results section provides an understanding of the reliability and performance of the computational models by contrasting experimental data with numerical predictions. The jet exit region, the dispersion behavior of the coolant jets, and the flow mixing mechanisms merit close scrutiny. The flow vector was zoned across six mixed streamwise and spanwise measurement planes to get statistically significant mean time numbers. Each combined plane corresponds to a different measurement, so there are six sets of measurements. This arrangement guarantees crossflow fluid travel throughout the full measurement domain, including all six planes.

4.2. Flow calculation results

4.2.1. Comparison between experimental and the numerical results of reduced speeds

Simulations of the mean and turbulent velocity profiles along the centerline (x–z baseline) were conducted over the flat plate and compared with experimental data, as seen in Fig. 10 and Fig. 11, to help one visualize the interaction dynamics between the coolant jets and the crossflow. With an eye on determining which model best reflects the complex jet–crossflow interactions from the jet exit to the far downstream region, these comparisons seek to evaluate the predictive accuracy of the two models of Standard turbulence k-ε and SSTs with respect to the experimental PIV data. The comparisons were made at a blowing ratio of M = 2.

At several streamwise locations X/D = −2, 0, 2, 8, 22, and 30 the graphs show the decreased axial (U/U_e) and vertical mean velocity components (V/U_e) across the spanwise symmetry plane (Z/D = 0). The examination shows that the jet's momentum significantly disturbs and deflects the crossflow as it approaches the jet exit. Significant differences between the experimental data and numerical calculations are observed in these near-wall regions, particularly in the prediction of axial velocity profiles. Although the SST model closely fits experimental trends across most sites, both turbulence models tend to overpredict the decrease in axial velocity near the wall. There are clear differences between the two models right after the jets, especially in how well they capture the regions where the flow separates and reattaches. The better performance of the SST model is ascribed to its greater ability to handle energy generation and transport processes associated with coherent structures, yet it has a tendency to somewhat overestimate their impact.

Conversely, the standard k–ε model omits important flow characteristics, especially in the downstream area, where it forecasts insufficient jet dispersion and little lateral dispersion. Particularly in regions affected by jet–crossflow interaction dynamics, this deficit might account for the clear departure from experimental data.

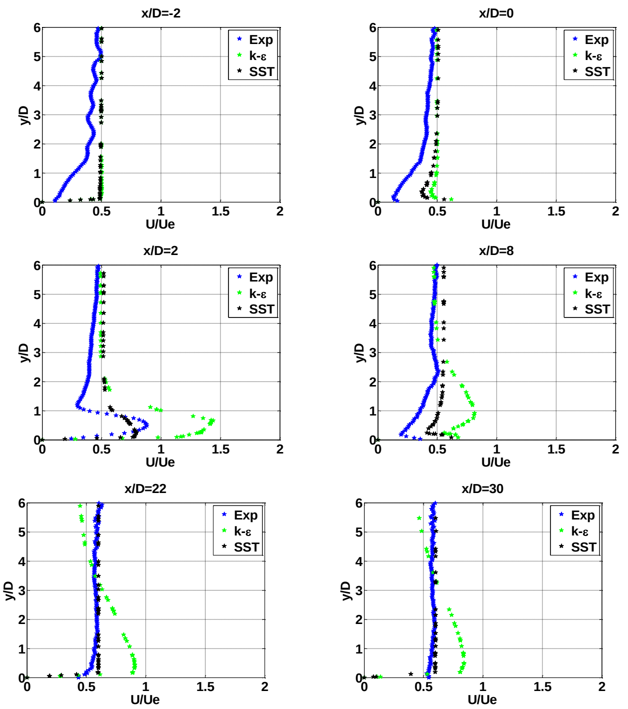

Fig. 10. Comparison of experimental and numerical results of reduced mean velocity profiles (U/U_e) along the central plane Z/D = 0

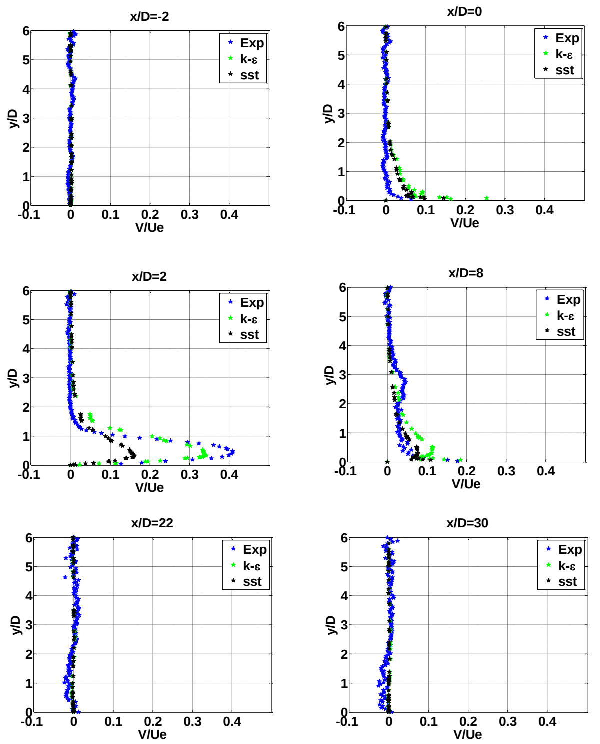

Fig. 11. Comparison of experimental and numerical results of reduced mean velocity profiles (V/Ue) along the central plane Z/D = 0

4.2.2. Comparison of turbulence energy along the axis of the jet

For a jet shot into a boundary layer at an injection rate of M = 2.0, Fig. 12 shows the contours of turbulent kinetic energy (TKE) predicted by the two models, Standard turbulence k–ε (Fig. 12a) and SSTs (Fig. 12b), compared to the experimental PIV measurements (Fig. 12c). The visualizations show how a fully turbulent jet interacts with the flow in the boundary layer. Though both computational models reflect the basic characteristics of the jet development and turbulence generation, neither matches the experimental results well. Near-wall areas and the degree of turbulent diffusion are where inconsistencies are especially obvious. Compared to the k-ε model, which often underestimates the spatial extent and intensity of turbulent structures, the SST model captures the shear-layer turbulence of the jet more accurately. Still, neither model can correctly reproduce the precise TKE distribution seen in the PIV data, therefore limiting their ability to capture the complex jet–crossflow interaction at this blowing ratio.

4.2.3. The contour lines of velocity magnitude derived from simulation outputs

Figure 13 shows the reduced mean velocity profiles from the three-dimensional (3D) simulations of the jet–crossflow interaction in the spanwise direction (Z/D) to investigate the lateral spreading behavior of the coolant jet. To evaluate the degree of jet diffusion and symmetry of the flow field, velocity profiles are derived at two streamwise locations, X/D = 12 and X/D = 16, then plotted along the spanwise direction. These graphs show how well the jet spreads and how well the fluid mixes as it moves away from the injection point.

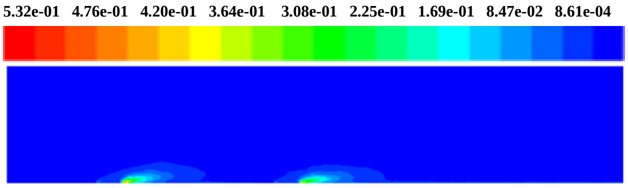

(a) Contours of the kinetic energy of turbulence obtained by the turbulence model k–ε

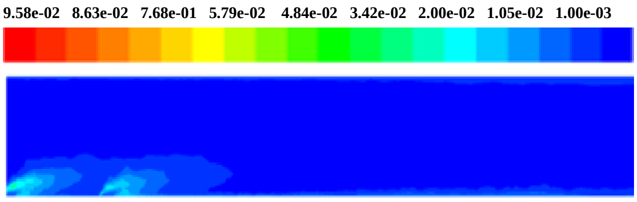

(b) Contours of the kinetic energy of turbulence obtained by the turbulence model SST

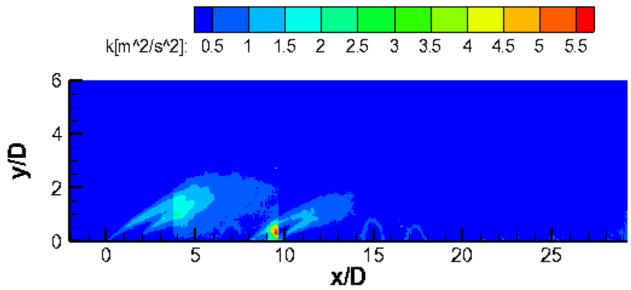

(c) Contours of the kinetic energy of turbulence obtained by the PIV

Fig. 12. Contours of the kinetic energy obtained by numerical calculation and by experiment

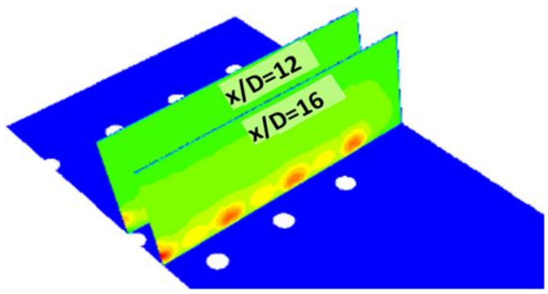

Fig. 13. Center planes x/D = 12 and x/D = 16

Transverse-plane measurements using the PIV technique could not be performed due to limitations in camera placement and movement. Therefore, only quantitative data from Fig. 14 for both turbulence models may be examined. The image shows isocontours of constant reduced velocity, which help show how the coolant film moves laterally. In terms of both the shape and intensity of the velocity contours, the standard k–ε and SST models provide rather similar estimates. For instance, the SST model yields a range of 1.79 to 4.87 for the reduced axial velocity U/Ue at X/D = 16; the k–ε model yields a range of 1.78 to 4.86. The RSM forecasts a range of 2.35 to 4.70 for comparison, showing a somewhat improved ability to capture the peak velocity zones. These findings imply that, while the k–ε and

SST models provide generally similar predictions, they might underpredict certain flow structures compared to more sophisticated models such as the RSM.

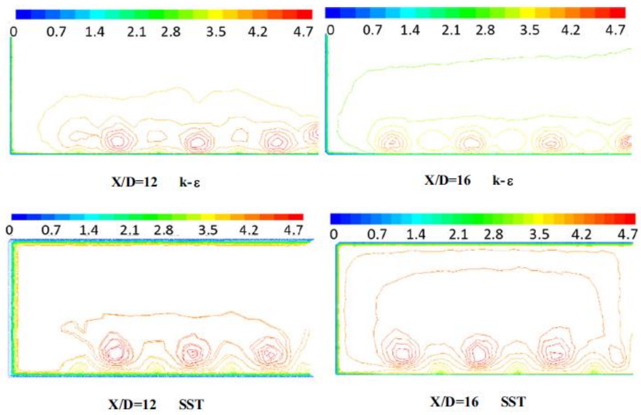

Fig. 14. Contours of velocity magnitude for k–ε and SST models in X/D = 12 and X/D = 16 center plane

Conclusions

This study experimentally and numerically examined the interaction of multiple staggered cooling jets with a turbulent crossflow representative of gas turbine blade film cooling at a blowing ratio of M = 2. Comparisons between PIV measurements and RANS simulations indicate that the SST turbulence model predicts jet penetration, velocity decay, and turbulence distribution more accurately than the standard k–ε model, particularly in the near-hole region dominated by strong shear and recirculation. The k–ε model was found to overestimate near-wall velocities and to underestimate jet spreading, potentially leading to non-conservative cooling predictions. For engineering applications, the SST model is recommended for CFD-based analysis and the preliminary design of multirow film-cooling configurations operating at moderate blowing ratios, whereas the standard k–ε model should be used only for qualitative assessments or supported by experimental validation. Future work should focus on the application of advanced turbulence modeling approaches, such as Reynolds stress models or hybrid RANS LES methods, to better capture unsteady jet-crossflow interactions. In addition, coupling aerodynamic analysis with thermal simulations is recommended to directly evaluate film-cooling effectiveness and heat transfer performance under realistic operating conditions.

Bibliography

[1] Amroune S, Belaadi A, Menasri N, Zaoui M, Mohamad B, Amin H. New approach for computer-aided static balancing of turbines rotors. Diagnostyka. 2019;20(4). https://doi.org/10.29354/diag/114621
[2] Amroune S, Mohamad B, Moussaoui M, Saaidi H. Geometric regeneration and mechanical analysis of a gas turbine blade type Frame 9001 GE. Eng Solid Mech. 2018;6(2):105-112. https://doi.org/10.5267/j.esm.2018.3.003
[3] Andreopoulos J, Rodi W. Experimental investigation of jets in a crossflow. J Fluid Mech. 1984;138:93-127. https://doi.org/10.1017/S0022112084000057
[4] Baghoolizadeh M, Rostamzadeh-Renani R, Rostamzadeh-Renani M, Toghraie D. A multi-objective optimization of a building's total heating and cooling loads and total costs in various climatic situations using response surface methodology. Energy Rep. 2021;7:7520-7538. https://doi.org/10.1016/j.egyr.2021.10.092
[5] Balaji K, Praveen R, Saravanan R, Karthik K. Review of cooling effect on gas turbine blade. Int Conf Syst Sci Control Commun Eng Technol. 2016;2:478-482.
[6] Barnoon P, Toghraie D, Mehmandoust B, Fazilati MA, Eftekhari SA. Natural-forced cooling and Monte-Carlo multi-objective optimization of mechanical and thermal characteristics of a bipolar plate for use in a proton exchange membrane fuel cell. Energy Rep. 2022;8:2747-2761. https://doi.org/10.1016/j.egyr.2022.01.199
[7] Barnoon P, Toghraie D, Rostami S. Optimization of heating-cooling generators with porous components/cryogenic conductors on natural convection in a porous enclosure: using different two-phase models and single-phase model and using different designs. Int Commun Heat Mass Transf. 2020; 111:104472. https://doi.org/10.1016/j.icheatmasstransfer.2019.104472
[8] Berkache A, Dizene R. Numerical and experimental investigation of turbine blade film cooling. Heat Mass Transf. 2017;53(12):3443-3458. https://doi.org/10.1007/s00231-017-2062-z
[9] Cao N, Li X, Wu Z, Luo X. Effect of film hole geometry and blowing ratio on film cooling performance. Appl Therm Eng. 2020;165:114578. https://doi.org/10.1016/j.applthermaleng.2019.114578
[10] Chatzistefanou A, Tsentis S, Kalfas A. Synergetic and performance characteristics of a high-speed precooled propulsion concept. J Eng Gas Turb Power. 2025;147(2):021016. https://doi.org/10.1115/1.4066352
[11] Choi J, Choi J, Kwon H, Jang H, Park H. Experimental investigation of the film cooling performance by triangular-shaped thin plates on inclined cylindrical holes. Front Energy Res. 2022;10:981275. https://doi.org/10.3389/fenrg.2022.981275
[12] Czarnecki M, Gawron B, Kwiatkowski T, Urban J, Kowal J. GTM-120 micro gas turbine engine noise identification. Combust Engines. 2024;199(4):52-59. https://doi.org/10.19206/CE-189743
[13] Esfe MH, Toghraie D. Numerical study on the effect of solar radiation intensity on the fresh water productivity of solar still equipped with thermoelectric cooling system (TEC) for hot and dry areas of Semnan. Case Stud Therm Eng. 2022; 32:101848. https://doi.org/10.1016/j.csite.2022.101848
[14] Forster M, Weigand B. Experimental and numerical investigation of jet impingement cooling onto a concave leading edge of a generic gas turbine blade. Int J Therm Sci. 2021; 164:106862. https://doi.org/10.1016/j.ijthermalsci.2021.106862
[15] Guo T, Zheng W, Li G, Song D, Niu W, Zhang C et al. Protrusion-enhanced flow and heat transfer in jet impingement cooling: a combined study. Appl Ther Eng. 2026;288: 129631. https://doi.org/10.1016/j.applthermaleng.2025.129631
[16] He X, Li H, Zhao G, You R. Comparison of turbine blade film cooling efficiency between PSP and TLC techniques in a stationary wind tunnel. AIP Adv. 2021;11(1):015333. https://doi.org/10.1063/5.0030289

[17] Johnston JP, Mosier BP, Khan ZU. Vortex generating jets; effects of jet-hole inlet geometry. Int J Heat Fluid Flow. 2002;23(6):744-749. https://doi.org/10.1016/S0142-727X(02)00138-8

[18] Jones WP, Wille M. Large-eddy simulation of a plane jet in a cross-flow. Int J Heat Fluid Flow. 1996;17(3):296-306. https://doi.org/10.1016/0142-727X(96)00045-8

[19] Kong D, Zhang C, Ma Z, Liu C, Isaev SA, Guo T et al. Numerical study on flow and heat transfer characteristics of swirling jet on a dimpled surface with effusion holes at turbine blade leading edge. Appl Therm Eng. 2022;209: 118243. https://doi.org/10.1016/j.applthermaleng.2022.118243

[20] Leedom DH. Numerical investigation of film cooling fluid flow and heat transfer using large eddy simulations. Master's thesis. Baton Rouge: Louisiana State University. 2009. https://repository.lsu.edu/gradschool_theses/4261

[21] Menter FR. Two-equation eddy-viscosity turbulence models for engineering applications. AIAA J. 1994;32(8):1598-1605. https://doi.org/10.2514/3.12149

[22] Mohamad B, Ali M, Neamah H, Zelentsov A, Amroune S. Fluid dynamic and acoustic optimization methodology of a Formula-Student race car engine exhaust system using multilevel numerical CFD models. Diagnostyka. 2020;21(3): 103-111. https://doi.org/10.29354/diag/126562

[23] Mohamad B, Zelentsov A. 1D and 3D modeling of modern automotive exhaust manifold. J Serb Soc Comput Mech. 2019;13(1):80-91. https://doi.org/10.24874/jsscm.2019.13.01.05

[24] Stajuda L, Gnap J, Rymaniak Ł, Merkisz J. Composition, features, problems, and treatment related to cooling fluid – a review. Combust Engines. 2024;196(1):106-125. https://doi.org/10.19206/CE-169185

[25] Toghraie D, Alempour SM, Afrand M. Experimental determination of viscosity of water based magnetite nanofluid for application in heating and cooling systems. J Magn Magn Mater. 2016;417:243-248. https://doi.org/10.1016/j.jmmm.2016.05.092

[26] Vicano V, Huang W, Xu Z, Zhou W, Liu Y, He C. Experimental jet in crossflow analysis for the 777 shaped hole. Proceedings of the Global Power and Propulsion Society Forum. 2025. https://doi.org/10.33737/gpps25-tc-097

[27] Wang J, Zhao Z, Tian L, Ren X, Sundén B. Effects of hole configuration on film cooling effectiveness and particle deposition on curved surfaces in gas turbines. Appl Therm Eng. 2021;190:116861. https://doi.org/10.1016/j.applthermaleng.2021.116861

[28] Wang J, Yu S, Bai G, Jiang C, Kang J. Experimental and simulation investigation on flow structures and energy transfer of rectangular jets with different aspect-ratios in cross-flow. Eng Appl Comput Fluid Mech. 2025;19(1):2507715. https://doi.org/10.1080/19942060.2025.2507715

[29] Yang D, Qiu M, Wu H, Li Y, Jiang Z, Huang K. Temperature uniformity characteristics of array jet impingement cooling with the maximum cross-flow scheme. Int J Therm Sci. 2023;187:108161. https://doi.org/10.1016/j.ijthermalsci.2023.108161

[30] Yao Y, Zhang J, Yang Y. Numerical study on film cooling mechanism and characteristics of cylindrical holes with branched jet injections. Propuls Power Res. 2013;2(1):30-37. https://doi.org/10.1016/j.jppr.2012.12.001

[31] Yuan LL, Street RL. Large eddy simulation of a jet in crossflow. Proc ASME Int Mech Eng Congr Expo, Fluids Eng. Atlanta. 1996:253-260. https://doi.org/10.1115/IMECE1996-0983

Prof. Amar Berkache, DSc., DEng. – Faculty of Technology, University of M'sila, M'sila, Algeria.
e-mail: *amar.berkache@univ-msila.dz*

Aram Mohammed Ahmed, DEng. – College of Oil and Gas Techniques Engineering/Kirkuk, Northern Technical University, Kirkuk, Iraq.
e-mail: *aram.mohammed@ntu.edu.iq*

Prof. Salah Amroune, DEng. – Department of Mechanical and Industrial Engineering, Faculty of Technology, University of M'sila, M'sila, Algeria.
e-mail: *salah.amroune@univ-msila.dz*

Firas F. Qader, Meng.- Kirkuk Technical Engineering College, Northern Technical University, Kirkuk 36001, Iraq.
e-mail: *firas.f.qader@ntu.edu.iq*

Barhm Mohamad, DEng., Assist. Prof. – Department of Petroleum Technology, Koya Technical Institute, Erbil Polytechnic University, Erbil, Iraq.
e-mail: *barhm.mohamad@epu.edu.iq*